PAPER

Effect of pressure on the structural, electronic and mechanical properties of ultraincompressible W₂B

Zhen Qin, Weiguang Gong, Xianqi Song, Menglong Wang, Hongbo Wang [ID] *
and Quan Li [ID] *

The crystal structures of W₂B have been extensively investigated by the swarm structure searching method at ambient and high-pressure conditions. Our calculated thermodynamic enthalpy data suggests that the tetragonal phase with *I4/m* symmetry is the most stable at 0–50 GPa. The theoretical elastic properties and phonon spectroscopy confirmed that *I4/m* W₂B is both mechanically and dynamically stable. The calculated band structure and density of states show that *I4/m* W₂B is metallic and the electronic properties are sensitive to changes in external pressure with the occurrence of an electronic topological transition. The simulated high elastic modulus, hardness and strain–stress relationships reveal that W₂B exhibits excellent ultraincompressible properties and high strength. The combination of superior conductivity and mechanical properties reveals that W₂B can be used for hard coatings and electrical measurements.

1. Introduction

Tungsten borides are exemplary materials with covalent-bonds formed by light elements (LE) and transition metals (TM), and exhibit excellent performance in terms of their chemical inertness, hardness, and stability; thus, they have been widely used as cutting tools and wear-resistant coatings.[1–4] The high hardness and high strength of these TM borides benefit from not only the contributors to the macroscopic hardness, but also the determinants of the relative hardness of structurally related borides and the anisotropic hardness of W borides.[4–13] It is widely expected that with higher concentration of the B atoms, the compounds will possess higher hardness. Several tungsten borides with outstanding mechanical properties have been synthesized with inexpensive starting materials, and economical experimental conditions (*e.g.*, ambient-pressure and high temperature conditions).[5,14–16] A comprehensive understanding of the mechanical mechanism for tungsten borides with various boron content has been plagued by the complex structural arrangements due to their flexible bonding ability. Recently, the structural determination of these tungsten borides has been widely explored by the latest first-principles structural search techniques and Rietveld refinement of the X-ray powder patterns.[17–19] It is essential to understand the structural and mechanical response under various loading conditions and examine the influence of B content on the strength and hardness of these tungsten borides. Based on the prototypes of

boron-rich tungsten borides, our previous calculations show that WB₂ phases with relatively lower boron content exhibit better overall strength, and the increase in the B content does
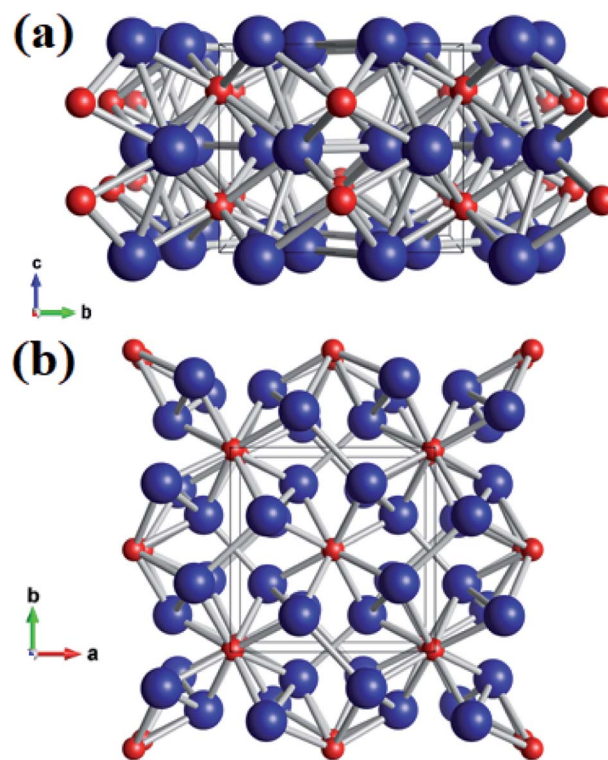

Fig. 1 (a) Front view and (b) top view of the *I4/m* structure of W₂B under ambient pressure. Large blue and small red spheres represent tungsten and boron atoms, respectively.

Key Laboratory of Automobile Materials of MOE, State Key Laboratory of Superhard Materials, Department of Materials Science, Jilin University, Changchun 130012, China. E-mail: liquan777@jlu.edu.cn; whb2477@jlu.edu.cn
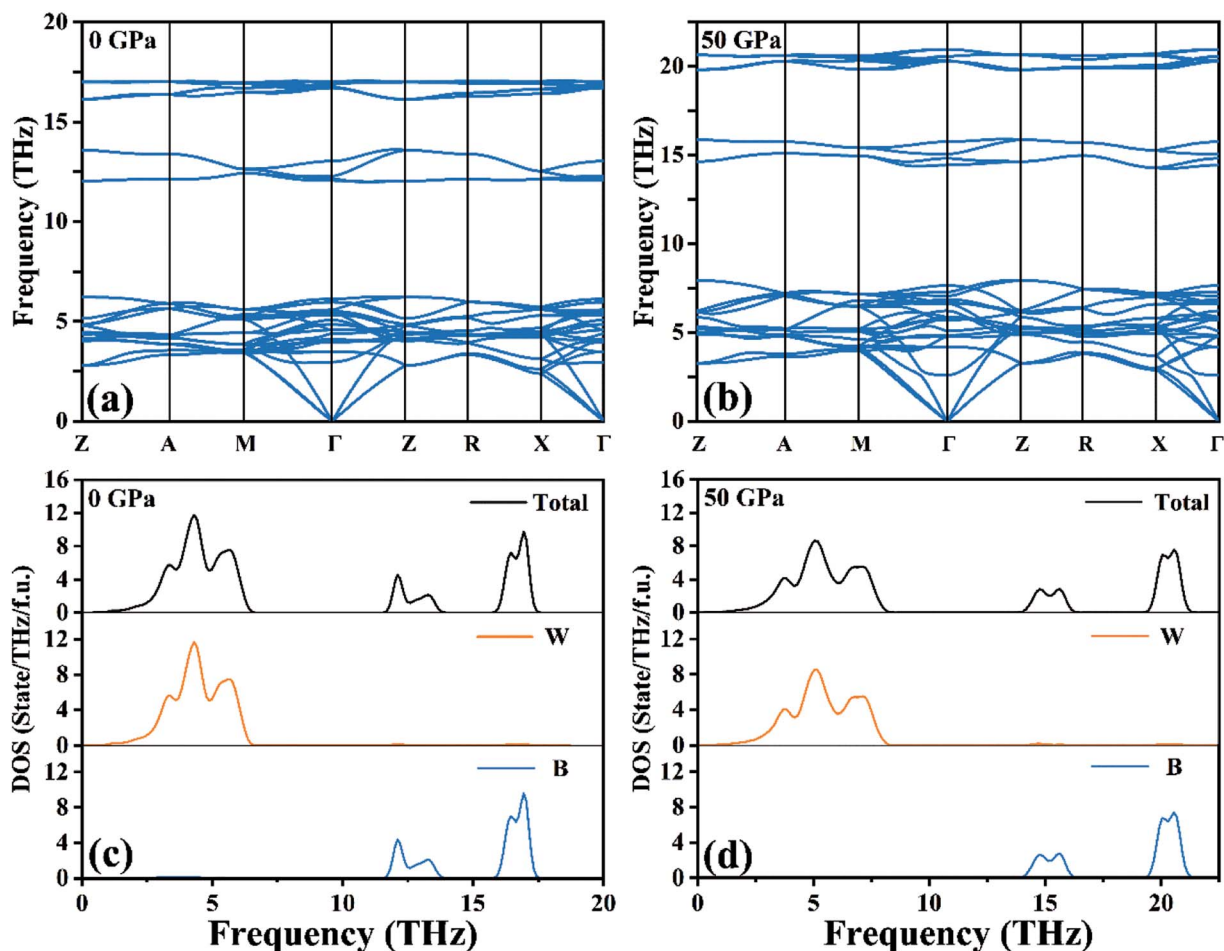
Fig. 2 (a and b) Calculated phonon dispersion curves and (c and d) phonon density of states for W_2B at 0 GPa and 50 GPa, respectively.

not lead to higher strength and hardness.[19] A pressing task is to explore the fundamental atomistic mechanisms for the structural and mechanical response under various conditions for tungsten borides with the lowest B content ratio, *i.e.*, W_2B (γ-W_2B). The measured Vickers hardness of W_2B reaches 24 GPa at 0.49 N.[20] W_2B has been thought to have a tetragonal Al_2Cu-type structure with $I4/mcm$ symmetry for several decades.[8,21–23] However, our recent results have clarified and corrected previous structural assignments for W_2B[18] and identified a new $I4/m$ structure that is energetically stable at ambient conditions. Thus, the corresponding physical properties and functional performance of γ-W_2B should be reexamined. It is known that these potential superhard materials mainly serve under load conditions, *e.g.*, high pressure, which is a very effective means to modulate the crystal structures and physical properties for condensed materials.[24–27] Therefore, we have systematically explored the underlying structural, electronic and mechanical properties for W_2B at ambient and high-pressure conditions. Our calculations show that $I4/m\bar{4}u$ W_2B is the most stable structure at the entire pressure range of 0–50 GPa. Dynamical stability has been identified by the calculated phonon spectrum. The calculated high bulk modulus, shear modulus and hardness data show that W_2B possesses excellent mechanical properties. Furthermore, W_2B exhibits a metallic feature, and

the band structure is sensitive to changes in external pressure. A pressure-induced electronic topological transition has been predicted in W_2B, which can cause anomalies in a wide range of physical properties, such as resistivity, thermoelectric power, and the Hall coefficient. The calculated stress–strain results show that W_2B has small elastic anisotropy in the elastic range. W_2B, with both superior conductivity and mechanical properties, can be used for many applications such as hard coatings and electrical measurements.

2. Computational methods

The first-principles energetic calculations were performed using the density functional theory with the Perdew–Burke–Ernzerhof generalized gradient approximation (GGA) exchange-correlation potential[28] as implemented in the Vienna ab initio simulation package (VASP).[29] Global structural predictions were performed using the CALYPSO method,[30–33] which has successfully predicted the stable and metastable structures of various systems.[34–36] The ion–electron interaction was treated by the projector augmented-wave (PAW) technique,[37] where $5d^4 6s^2$ and $2s^2 2p^1$ were adopted as valence electrons for W and B atoms, respectively. The electronic wave functions were expanded in a plane-wave basis set. The desirable cutoff energy
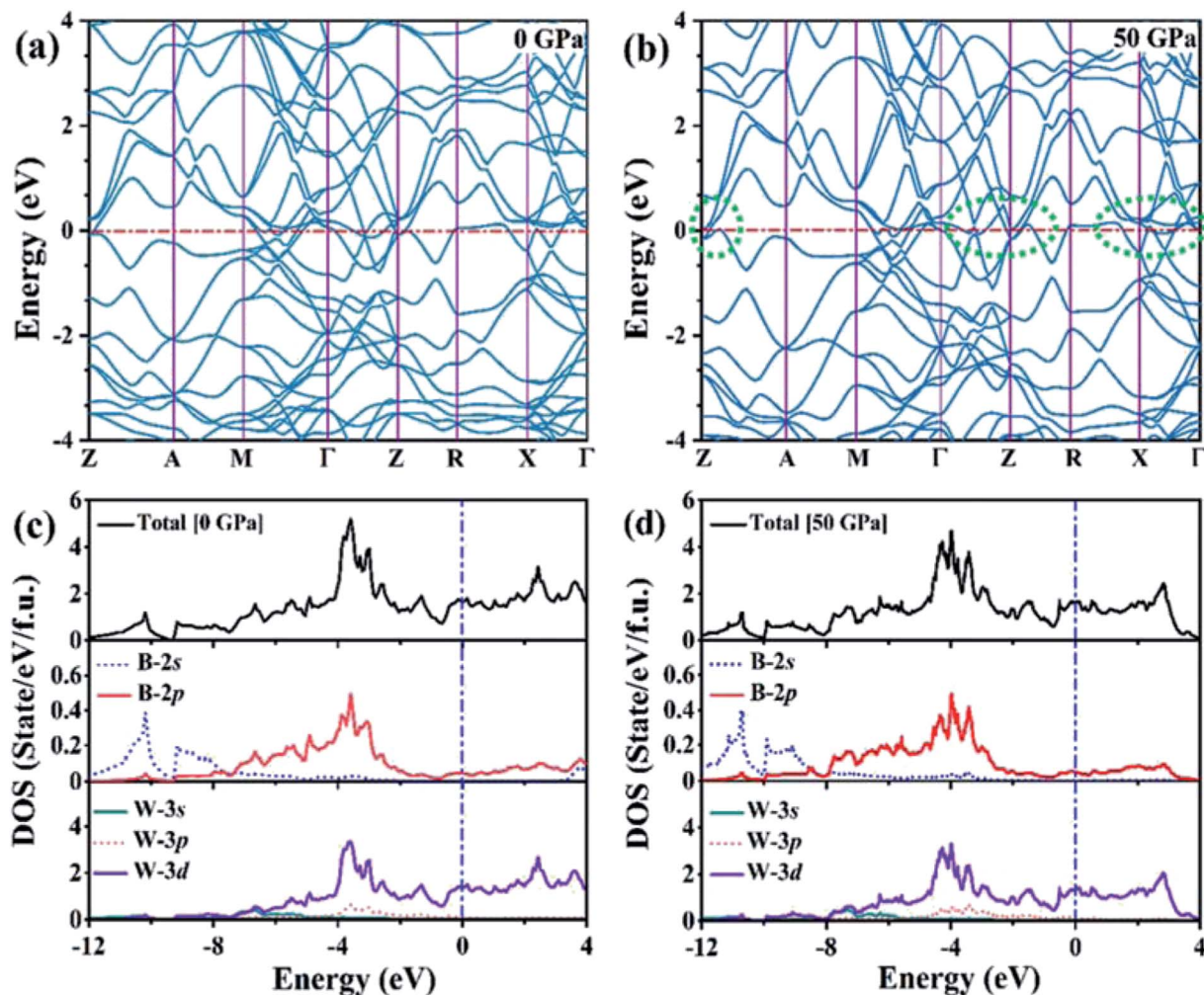
Fig. 3 (a and b) Electronic band structures and (c and d) electronic total and partial DOS of the W_2B at 0 GPa and 50 GPa, respectively. The zero of the energy coincides with the Fermi level. The green dashed circles highlight the changes of electronic band structures near the Fermi level.

of 600 eV and appropriate Monkhorst–Pack k point meshes[16] for Brillouin zone sampling were chosen to ensure that the total energies converged to be better than 1 meV per atom for all cases. Phonon calculations were conducted using a supercell approach as implemented in the PHONOPY code.[38] Elastic constants were calculated by adopting the strain–stress method and the three-dimensional models of modulus were built using Elastic Anisotropy Measures (ELAM) code[39] to manifest anisotropy of the perfect single crystal. The bulk (B) and shear moduli (G) for corresponding isotropic polycrystalline were derived from the Voigt–Reuss–Hill averaging scheme.[40] The relaxed loading path and quasi-static ideal strength were determined using a previously established method[41] with the lattice vectors manually deformed in the direction of the applied strain and the other independent strain tensors simultaneously relaxed.

3.   Results and discussion

Using the variable-cell CALYPSO method, the structural search for W_2B was performed with cell sizes of 1–4 formula units at 0–50 GPa. The current analysis on thermodynamic enthalpy

confirmed that the tetragonal phase with $I4/m$ symmetry is most stable at ambient and high-pressure conditions. Lattice parameters of the $I4/m$ structure from theoretical calculations are $a = b = 5.580$ Å and $c = 4.756$ Å, accompanied by equilibrium atomic Wyckoff positions of 8h (0.176, 0.664, 0.0) for W atoms and 4e (0.0, 0.0, 0.221) for B atoms. Perspective structural screenshots from diverse views of W_2B are shown in Fig. 1. Each tungsten atom is surrounded by four boron atoms as well as three tungsten atoms with two approximately equal W–W bond lengths of 2.688 and 2.693 Å [Fig. 1(a)], which are slightly smaller than those in pure tungsten metal (2.747 Å). Furthermore, each boron atom has an eightfold coordinate with tungsten atoms with two analogous bond lengths of 2.365 and 2.420 Å [Fig. 1(b)].

Based on harmonic approximation, the calculated phonon dispersion curves exhibiting vibration modes of the $I4/m$ structure of W_2B have been shown in Fig. 2(a). There is no imaginary frequency in the entire Brillouin zone, $i.e.$, all the phonon frequencies are positive, which demonstrates that the $I4/m$ structure of W_2B is dynamically stable under ambient pressure. The current results are in good agreement with
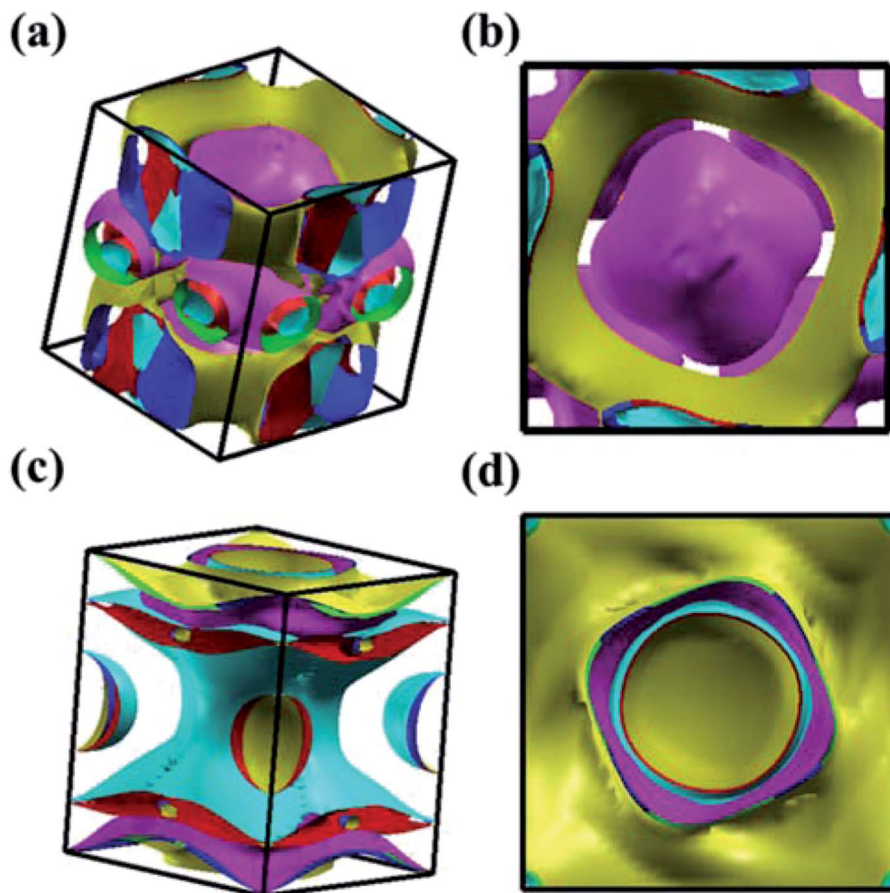
Fig. 4 Screenshots for the calculated Fermi surface of $I4/m$ W_2B from different directions at 0 GPa (a and b) and 50 GPa (c and d), respectively.

previous calculations.[42] We have further checked the phonon spectra for $I4/m$ symmetry of W_2B at high-pressure conditions to further identify its dynamical stability [Fig. 2(b)]. The blue shift of phonon peaks with the increase in pressure originates from the enhanced force constants affected by atomic distances. An interesting phenomenon is found in the phonon dispersion curves of the W_2B. They possess apparent gaps between the high and low frequency areas. We further analyzed the contribution of tungsten and boron atoms to phonon frequency by means of the phonon density of the states of W_2B, as shown in Fig. 2(c and d). Our results show that the vibrations of tungsten atoms and boron atoms correspond to low and high phonon frequency areas, respectively, which stems from the greater mass of the tungsten atom than that of the boron atom.

We analyzed the electronic band structure, density of states (DOS) and topological nature of the Fermi surface for exhibiting electronic properties of the $I4/m$ phase at atmospheric and high pressure. The distinct crossover behavior between the valence and the conduction bands indicates that $I4/m$ W_2B is metallic, as shown in Fig. 3. Our results, as shown in Fig. 3(a), indicate that the delocalized W-3d orbitals dominate the electronic density of the states around the Fermi level. The substantial overlap of the W-3d and B-2p states [Fig. 3(c and d)] demonstrates the strong covalent bonding states between boron atoms and tungsten atoms. It is noted that a deep energy valley (pseudogap) is shown in the calculated electronic DOS below

the Fermi level at about −0.7 eV. It has been confirmed that the pseudogap separates the localized and delocalized electrons, where the electrons of the valence bands above (below) the pseudogap are delocalized (localized). The presence of the pseudogap indicates that the covalent bonds play the dominant role in W_2B, which has been to effectively enhance its mechanical properties, *e.g.*, high bulk modulus, shear modulus, and hardness. With the increase in pressure, the crossing behavior of the electronic band structure near the Fermi energy evidently changed near the Z point and X–Γ directions, which are highlighted by the dotted circles in Fig. 3(b). The significant changes in the Fermi surface profiles in Fig. 4 demonstrate the occurrence of a pressure-induced electronic topological transition, which causes anomalies in a wide range of physical properties, such as resistivity, thermoelectric power, and the Hall coefficient. The 3D Fermi surfaces [Fig. 4], with some visible nesting features, are very complex in the entire Brillouin zone, which may be responsible for the superconductivity of W_2B at 3.1 K.[43]

The elastic constants of the $I4/m$ W_2B were calculated by the strain–stress method at a small strain of 0.3%. Our results show that the independent elastic constants satisfy the mechanical stability criteria,[44] suggesting that $I4/m$ W_2B is elastically stable. In order to visually reflect anisotropy of elastic moduli, the three-dimensional models of linear compressibility, Young's modulus, Poisson's ratio and shear
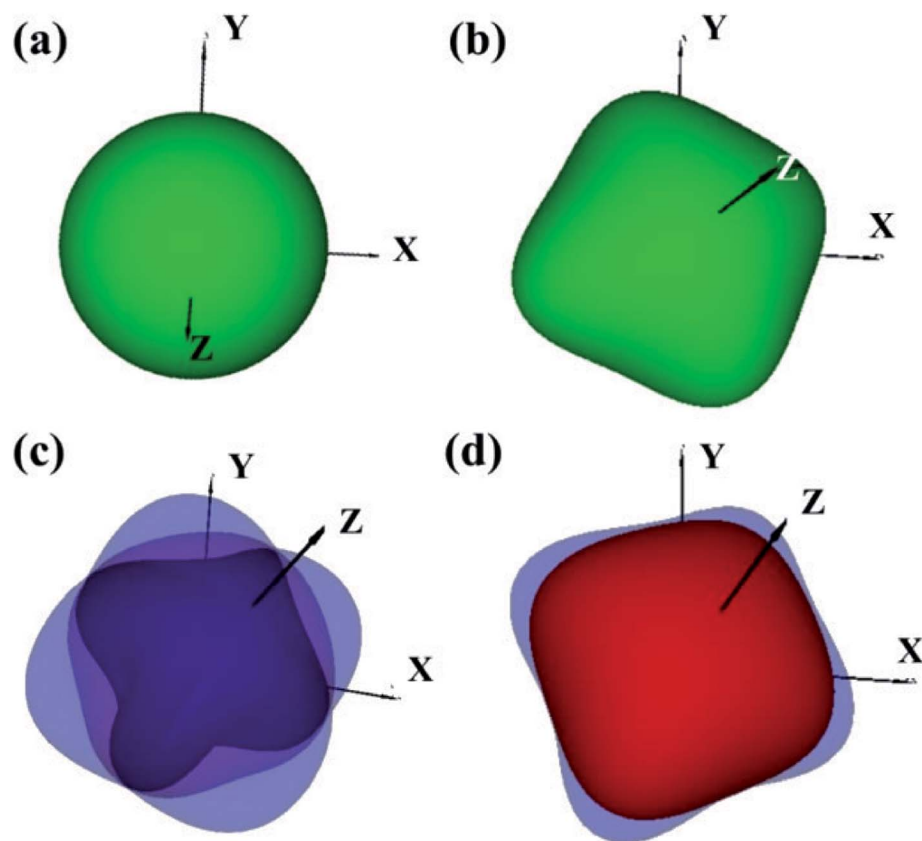
Fig. 5 3D representations of elastic properties based on theoretical elastic stiffness constants C_{ij} of W_2B at a small strain of 0.3% (near the equilibrium). (a) Uniaxial compression modulus representation surfaces. (b) Young's modulus E representation surfaces. (c) Poisson's ratio v representation surfaces. (d) Shear modulus G representation surfaces.

Table 1 The calculated elastic constants C_{ij} (GPa), bulk modulus B (GPa), shear modulus G (GPa), Young's modulus E (GPa), Poisson's ratio P_r and Vickers hardness H_v (GPa) of W_2B

Phase	Pressure	C_{11}	C_{33}	C_{44}	C_{66}	C_{12}	C_{13}	B	G	E	P_r	H_v
$I4/m$	0 GPa	568	550	156	178	205	237	338	165	426	0.29	15.1
	50 GPa	799	756	226	269	302	352	485	234	605	0.29	19.1

modulus were calculated. As shown in Fig. 5, W_2B exhibits excellent mechanical properties with low elastic anisotropy at small strain. The simulated bulk modulus, shear modulus and Young's modulus of W_2B reach 338.5, 165.0 and 425.7 GPa, respectively, as listed in Table 1. The theoretical elastic properties show that the W_2B exhibits an unusual incompressibility, but is relatively weak to resist shear deformation. Poisson's ratio has also been calculated to describe the response of the transverse strain to the longitudinal strain. The calculated Poisson's ratio (P_r) reaches 0.29, indicating that W_2B is a typical isotropic engineering material ($0.2 < P_r < 0.5$) near the equilibrium, and its interatomic forces are predominantly central forces.[45] Based on the revised hardness model,[46,47] the simulated Vickers hardness value of the $I4/m$ structure is 15.1 GPa, which is comparable to that of aluminum nitride (AlN, 15–17 GPa).[48,49] Our results show that pressure significantly enhances the mechanical properties of

W_2B, as listed in Table 1, which is a key requirement for the application of hard materials.

We have systematically investigated the ideal strength for $I4/m$ W_2B in various tension and shear directions at large strain by first-principle calculations. The stress response relationships along diverse crystallographic directions are shown in Fig. 6. The weakest tensile stress for W_2B appears in the [111] direction, accompanied by a numerical value of ideal strength of 29.6 GPa with the corresponding strain of 0.12. At small strains, the tensile stress appears to rise almost linearly with large slopes, indicating that the equilibrium structure possesses large elastic constants. The stress responses along different directions are almost identical at strains below 5%, which is consistent with the 3D representations of elastic properties [Fig. 5]. The minimum shear stress of 21.4 GPa for W_2B is obtained along the (101) [010] crystal orientation with a strain of 0.17. At small strains, the slopes of the shear stress–strain curve
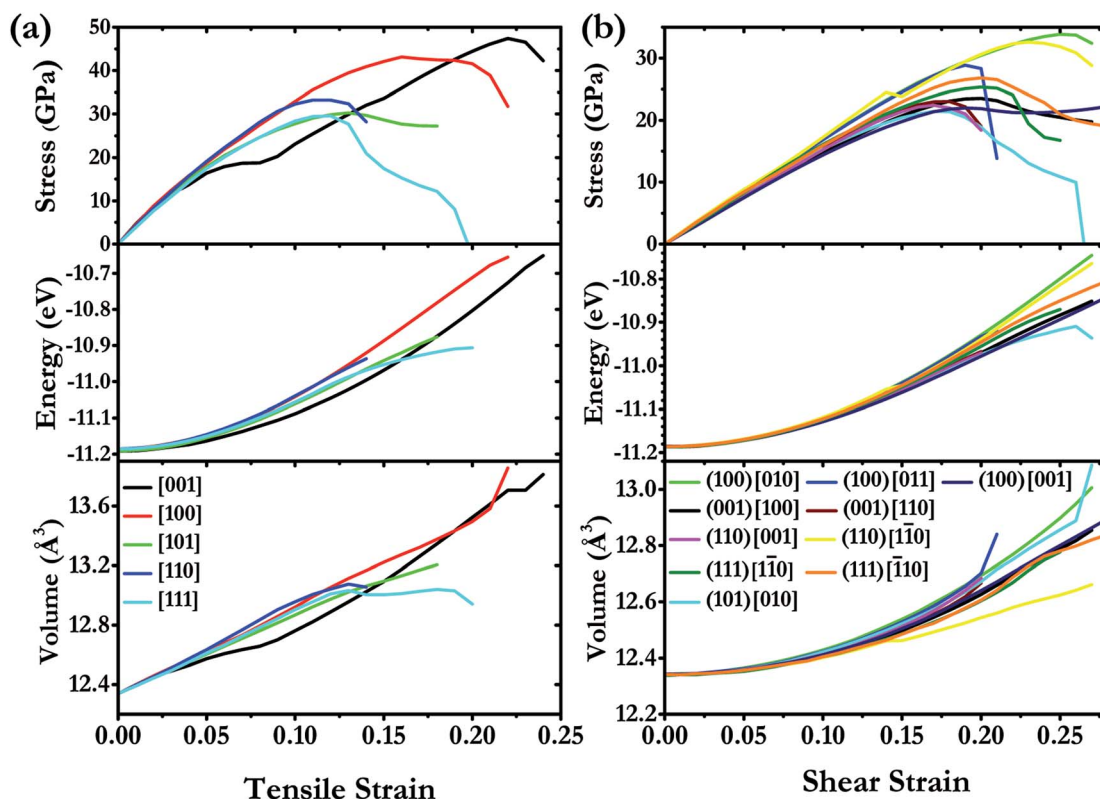
Fig. 6 (a) Calculated stress responses under tensile strain in various deformation directions and (b) calculated stress–strain curves on various shear sliding planes in different directions under pure shear deformation for W_2B at large strain under ambient pressure.

Table 2 Calculated peak stress values for W_2B with the corresponding strains

Tensile direction	Strain	Stress (GPa)	Shear direction	Strain	Stress (GPa)
[001]	0.22	47.4	(001) [100]	0.20	23.5
[100]	0.16	43.1	(001) [110]	0.18	23.0
[101]	0.13	30.3	(110) [1$\bar{1}$0]	0.23	32.6
[110]	0.12	33.3	(110) [001]	0.17	22.4
[111]	0.12	29.6	(111) [1$\bar{1}$0]	0.20	25.3
			(111) [$\bar{1}$10]	0.20	26.8
			(100) [010]	0.25	33.8
			(100) [011]	0.19	28.8
			(100) [001]	0.31	23.1
			(101) [010]	0.17	21.4

are gentler than those of the tensile stress–strain curves, which is consistent with the results of the elastic modulus near the equilibrium. The particular stress peaks as well as corresponding strains are listed in Table 2. It is noted that the strain–stress relations for traditional superhard materials, *e.g.*, diamond and c-BN, show a sudden break at stress peaks. Herein, W_2B presents a behavior of meandering decline that produces better ductility and extended elasticity than traditional superhard materials. In order to provide a more detailed description of the stress–strain process, we show the calculated energy and volume in various tensile, and shear deformation directions (Fig. 6). With an increase instress, the calculated energy increases monotonously and quickly. For tensile strain along the [111] direction, the volume increases first and then, the

enhancement is minor with a small variation in strain from 0.12 to 0.20. The shear process is the opposite, that is, the volume rises during the entire process along the (101) [010] crystal direction. Therefore, the failure mechanisms under tensile and shear deformations are significantly different.

4. Conclusion

In summary, we have systematically explored the thermodynamically stable structures for W_2B at pressure ranging from 0 to 50 GPa using the CALYPSO method. Our results indicate that W_2B with $I4/m$ symmetry is energetically and dynamically stable under atmospheric and high pressure. We have systematically studied the pressure effect on its intrinsic electronic

structure, elastic properties and stress response relations. The calculated band structure and density of states show that $I4/m$ W_2B is metallic and the electronic properties are sensitive to changes in external pressure with the occurrence of an electronic topological transition. The simulated high elastic modulus, hardness and strain–stress relationships reveal that W_2B exhibits excellent ultraincompressible properties, high hardness, and high strength. The superior conductivity and mechanical properties reveal that W_2B is expected to be used in many fields such as hard coatings for electrical devices or anvils of large volume press for electrical measurements.

Conflicts of interest

There are no conflicts to declare.

Acknowledgements

References

1 J. C. Crowhurst, A. F. Goncharov, B. Sadigh, C. L. Evans, P. G. Morrall, J. L. Ferreira and A. J. Nelson, *Science*, 2006, **311**, 1275–1278.

2 A. F. Young, C. Sanloup, E. Gregoryanz, S. Scandolo, R. J. Hemley and H. Mao, *Phys. Rev. Lett.*, 2006, **96**, 155501.

3 H. Y. Chung, M. B. Weinberger, J. B. Levine, A. Kavner, J. M. Yang, S. H. Tolbert and R. B. Kaner, *Science*, 2007, **316**, 436.

4 R. Mohammadi, A. T. Lech, M. Xie, B. E. Weaver, M. T. Yeung, S. H. Tolbert and R. B. Kaner, *Proc. Natl. Acad. Sci. U. S. A.*, 2011, **108**, 10958–10962.

5 M. Xie, R. Mohammadi, Z. Mao, M. M. Armentrout, A. Kavner, R. B. Kaner and S. H. Tolbert, *Phys. Rev. B: Condens. Matter Mater. Phys.*, 2012, **85**, 064118.

6 Q. Gu, F. Krauss and W. Steurer, *Adv. Mater.*, 2008, **20**, 3620–3626.

7 R. Kiessling, *Acta Chem. Scand.*, 1947, **1**, 893–916.

8 H. Itoh, T. Matsudaira, S. Naka, H. Hamamoto and M. Obayashi, *J. Mater. Sci.*, 1987, **22**, 2811–2815.

9 S. Okada, K. Kudou and T. Lundström, *Jpn. J. Appl. Phys.*, 1995, **34**, 226.

10 H. P. Woods, F. E. Wagner Jr and B. G. Fox, *Science*, 1966, **151**, 75.

11 M. Kayhan, E. Hildebrandt, M. Frotscher, A. Senyshyn, K. Hofmann, L. Alff and B. Albert, *Solid State Sci.*, 2012, **14**, 1656.

12 J. Lei, M. T. Yeung, P. J. Robinson, R. Mohammadi, C. L. Turner, J. Yan, A. Kavner, A. N. Alexandrova, R. B. Kaner and S. H. Tolbert, *J. Phys. Chem. C*, 2018, **122**, 5647–5656.

13 P. J. Robinson, G. Liu, S. Ciborowski, C. Martinez-Martinez, J. R. Chamorro, X. Zhang, T. M. McQueen, K. H. Bowen and A. N. Alexandrova, *Chem. Mater.*, 2017, **29**, 9892–9896.

14 H.-Z. Chen, Y.-Y. Zhang, X. Gong and H. Xiang, *J. Phys. Chem. C*, 2013, **118**, 2333.

15 M. Xie, R. Mohammadi, C. L. Turner, R. B. Kaner, A. Kavner and S. H. Tolbert, *Phys. Rev. B*, 2014, **90**, 104104.

16 H. J. Monkhorst and J. D. Pack, *Phys. Rev. B: Condens. Matter Mater. Phys.*, 1976, **13**, 5188.

17 A. T. Lech, C. L. Turner, R. Mohammadi, S. H. Tolbert and R. B. Kaner, *Proc. Natl. Acad. Sci. U. S. A.*, 2015, **112**, 3223–3228.

18 Q. Li, D. Zhou, W. Zheng, Y. Ma and C. Chen, *Phys. Rev. Lett.*, 2013, **110**, 136403.

19 Q. Li, D. Zhou, W. Zheng, Y. Ma and C. Chen, *Phys. Rev. Lett.*, 2015, **115**, 185502.

20 G. Akopov, M. T. Yeung and R. B. Kaner, *Adv. Mater.*, 2017, **29**, 1604506.

21 B. Armas and F. Trombe, *Sol. Energy*, 1973, **15**, 67–73.

22 S. Stadler, R. P. Winarski, J. M. MacLaren, D. L. Ederer, J. vanEk, A. Moewes, M. M. Grush, T. A. Callcott and R. C. C. Perera, *J. Electron Spectrosc. Relat. Phenom.*, 2000, **110–111**, 75–86.

23 E. Zhao, J. Meng, Y. Ma and Z. Wu, *Phys. Chem. Chem. Phys.*, 2010, **12**, 13158–13165.

24 Y. Zhou, Q. Xu, C. Zhu, Q. Li, H. Liu, H. Wang and J. S. Tse, *RSC Adv.*, 2016, **6**, 66721–66728.

25 F. Peng, Y. Sun, C. J. Pickard, R. J. Needs, Q. Wu and Y. Ma, *Phys. Rev. Lett.*, 2017, **119**, 107001.

26 Y. Ma, M. Eremets, A. R. Oganov, Y. Xie, I. Trojan, S. Medvedev, A. O. Lyakhov, M. Valle and V. Prakapenka, *Nature*, 2009, **458**, 182.

27 C. Chen, Y. Xu, X. Sun, S. Wang and F. Tian, *RSC Adv.*, 2014, **4**, 55023–55027.

28 J. P. Perdew, K. Burke and M. Ernzerhof, *Phys. Rev. Lett.*, 1996, **77**, 3865.

29 G. Kresse and J. Furthmüller, *Phys. Rev. B: Condens. Matter Mater. Phys.*, 1996, **54**, 11169.

30 Y. Wang, J. Lv, L. Zhu and Y. Ma, *Phys. Rev. B: Condens. Matter Mater. Phys.*, 2010, **82**, 094116.

31 Y. Wang, J. Lv, L. Zhu and Y. Ma, *Comput. Phys. Commun.*, 2012, **183**, 2063–2070.

32 H. Wang, Y. Wang, J. Lv, Q. Li, L. Zhang and Y. Ma, *Comput. Mater. Sci.*, 2016, **112**, 406–415.

33 X. Zhang, Y. Wang, J. Lv, C. Zhu, Q. Li, M. Zhang, Q. Li and Y. Ma, *J. Chem. Phys.*, 2013, **138**, 114101.

34 Y. Li, X. Feng, H. Liu, J. Hao, S. A. T. Redfern, W. Lei, D. Liu and Y. Ma, *Nat. Commun.*, 2018, **9**, 722.

35 X. Zhong, H. Wang, J. Zhang, H. Liu, S. Zhang, H.-F. Song, G. Yang, L. Zhang and Y. Ma, *Phys. Rev. Lett.*, 2016, **116**, 057002.

36 H. Zhang, Y. Li, J. Hou, K. Tu and Z. Chen, *J. Am. Chem. Soc.*, 2016, **138**, 5644–5651.

37 G. Kresse and G. D. JoubertKresse, *Phys. Rev. B: Condens. Matter Mater. Phys.*, 1999, **59**, 1758.

38 A. Togo, F. Oba and I. Tanaka, *Phys. Rev. B: Condens. Matter Mater. Phys.*, 2008, **78**, 134106.

39 A. Marmier, Z. A. Lethbridge, R. I. Walton, C. W. Smith, S. C. Parker and K. E. Evans, *Comput. Phys. Commun.*, 2010, **181**, 2102–2115.

40 R. Hill, *Proc. Phys. Soc., London, Sect. A*, 1952, **65**, 349.

41 D. Roundy, C. Krenn, M. L. Cohen and J. Morris Jr, *Phys. Rev. Lett.*, 1999, **82**, 2713.

42 M. Wang, C. Liu, M. Wen, Q. Li and Y. Ma, *Phys. Chem. Chem. Phys.*, 2017, **19**, 31592–31598.

43 G. F. Hardy and J. K. Hulm, *Phys. Rev.*, 1954, **93**, 1004–1016.

44 Z.-j. Wu, E.-j. Zhao, H.-p. Xiang, X.-f. Hao, X.-j. Liu and J. Meng, *Phys. Rev. B: Condens. Matter Mater. Phys.*, 2007, **76**, 054115.

45 H. Fu, D. Li, F. Peng, T. Gao and X. Cheng, *Comput. Mater. Sci.*, 2008, **44**, 774–778.

46 X.-Q. Chen, H. Niu, D. Li and Y. Li, *Intermetallics*, 2011, **19**, 1275–1281.

47 Y. Tian, B. Xu and Z. Zhao, *Int. J. Refract. Met. Hard Mater.*, 2012, **33**, 93–106.

48 D. M. Teter, *MRS Bull.*, 1998, **23**, 22–27.

49 F. Gao, J. He, E. Wu, S. Liu, D. Yu, D. Li, S. Zhang and Y. Tian, *Phys. Rev. Lett.*, 2003, **91**, 015502.